**EPJ manuscript No.**
(will be inserted by the editor)

# Structural and magnetic properties of [Er|Tb] multilayers

J. Voigt[1,2], E. Kentzinger[1], U. Rücker[1], W. Schweika[1], D. Wermeille[3], W. Schmidt[1,4], and Th. Brückel[1]

[1] Institut für Festkörperforschung, Forschungszentrum Jülich GmbH, 52425 Jülich, Germany
[2] Labor für Neutronenstreuung, Paul Scherrer Institut, 5232 Villigen-PSI, Switzerland
[3] Ames Laboratory-US DOE and Department of Physics and Astronomy, Iowa State University, Ames, Iowa 50011
[4] Institute Laue-Langevin, BP 156, F-38042 Grenoble Cedex 9, France

the date of receipt and acceptance should be inserted later

**Abstract.** We have investigated the structural and magnetic properties of [Er|Tb] multilayers by different scattering methods. Diffuse x-ray scattering under grazing incidence reveals the interface structure in [Er|Tb] bilayers and trilayers, indicating vertically correlated roughness between the Er and Tb interfaces. The magnetic properties of $[Er_{n_{Er}}|Tb_{n_{Tb}}]$ superlattices have been studied as a function of the superlattice composition (indices denote the number of atomic layers). Coupled ferromagnetic structures exist in all investigated samples. The phase transition temperature varies with the Tb layer thickness. Modulated magnetic order is short range for all samples beside the $[Er_{20}|Tb_5]$ superlattice, the sample with the smallest Tb layer thickness. We observe dipolar antiferromagnetic coupling between single ferromagnetic Tb layers in all samples, with the onset of this ordering depending on the Tb layer thickness. Due to competing interactions, exchange coupling is limited to the interface near region. Therefore long range modulated magnetic order is observed in the $[Er_{20}|Tb_5]$ superlattice only, where the interface regions overlap. The distinct differences to the magnetic structure of an $Er_{0.8}Tb_{0.2}$ alloy film are explained by a highly anisotropic arrangement of neighbouring atoms due to the correlated roughness.

**PACS.** 7 5.75.+a, 75.25.+z, 61.18.Fs

## 1 Introduction

The discovery of magnetic interlayer exchange coupling [1,2] initiated strong research activities in the field of rare earth superlattices. A comprehensive review of the different coupling mechanisms is given in [3]. Most studies are concerned with the exchange coupling across non magnetic spacers. More recent studies report on systems containing two magnetic rare earth metals [4–7] showing a variety of new magnetic phases.

The present study concerns the system [Er|Tb]. Mainly as a result of the crystal field anisotropy, the two elements Er and Tb exhibit fairly different magnetic structures in the bulk. Therefore one might expect complex magnetic structures in superlattices composed from these materials. We attempt to clarify the role of competing anisotropies and proximity by a systematic variation of the superlattice composition.

The magnetic structure in rare earth elements is determined by the subtle balance between RKKY interaction, crystal field anisotropy and magneto-elastic interactions. The RKKY interaction, i. e. the coupling of localised $4f$ magnetic moments via conduction band electrons, leads to the formation of modulated magnetic structures throughout the series of heavy rare earth metals.

For Tb metal, the crystal field anisotropy forces the magnetic moments to lie within the basal plane of the hexagonal lattice. In contrast, the magnetic moments are oriented preferably along the *c*-axis direction in Er. Phase transition temperatures differ strongly for the two elements. The Néel temperature $T_N$ for Tb is about 230 K. The basal plane helix is stable only in the small temperature range above 220 K. Below 220 K Tb is a simple basal plane ferromagnet.

Upon cooling, bulk Er orders first at $T_N$=81 K in a so called *c*-axis modulated structure, i. e. the magnetic moments are aligned along the *c*-direction, the size of the moment is identical in a given hexagonal basal plane and modulated sinusoidally along the *c*-direction. Below 54 K the basal plane component orders into a modulated structure with the same propagation vector. The magnetic modulation is not any more purely sinusoidal, but 'squares up' instead [8]. Between 34 K and 20 K the propagation vector locks in into a series of commensurate values. Finally, below 20 K, the *c*-axis component becomes ferromagnetic, while the basal plane component remains in a modulated order, yielding a cone structure.

The present paper is organised as follows: In section 2 we describe the sample preparation. The structural characterisation in section 3 was performed by means of x-ray scattering. Anomalous specular and off-specular x-ray scattering under grazing incidence reveals the interface

morphologies, while wide angle x-ray diffraction is used to probe the crystal quality. In section 4 we describe the magnetic structures determined by neutron diffraction. The X-ray resonance exchange scattering (XRES) data in section 5 provides element and electronic band specific information about the magnetic properties. Combining the results of neutron diffraction and XRES we propose different coupling mechanisms for the series of superlattices in section 6.

## 2 Sample preparation

Samples were prepared by means of molecular beam epitaxy (MBE). Following the approach described by Majkrzak et al. [9], the rare earth metal layers are deposited onto a buffer system [Sapphire($11\overline{2}0$) |Nb(110)|Y(0001)] with flat and clean Y (0001) surfaces. The layer thicknesses range from 250 to 1500 Å for the Nb layers and 600 to 1200 Å for the Y layer. The surface quality is controlled in situ by Low Energy Electron Diffraction (LEED) and Auger Electron Spectroscopy (AES). From AES, strong interdiffusion is found at Tb|Er interfaces at growth temperatures above 350°C. For growth temperatures below 270°C epitaxial growth of Er is suppressed as evidenced from the missing LEED pattern. Growth temperatures between 300 and 350 °C yield very good epitaxy, while interdiffusion cannot be the detected by AES. However, the sensitivity of AES is limited: Taking into account the chemical sensitivity this limits the surface coverage to 10 % for the 'buried' element.
To protect the rare earth layers from oxidation a final cap layer is deposited. For the grazing incidence measurements we use a 50 Å thick SiO layer (cp. [10]), while the superlattices for the magnetic studies are capped with a 200-300 Å thick Y layer [11].
For the interface characterisation we use bilayers and trilayers to keep the number of interfaces low. The structural properties of the superlattices used for the magnetic studies are summarised in table 1. For comparison with the different superlattices we produced a 6000 Å thick $Er_{0.8}Tb_{0.2}$ alloy by coevaporation of Er and Tb directly onto the Nb buffer layer.

## 3 Structural characterisation

The interface properties of [Er|Tb]-bilayers and [Tb|Er|Tb]-trilayers have been investigated by diffuse x-ray scattering under grazing incidence. Fig. 1 shows measurements of the reflectivity (i. e. $\alpha_i = \alpha_f = \frac{2\theta}{2}$) and longitudinal diffuse scans (i. e. $\alpha_i = \frac{2\theta}{2} - \Delta$) for different photon energies as a function of the $Q_z$ component of the scattering vector, i. e. the component normal to the surface. $\alpha_i$, $\alpha_f$ denote the angles between the sample surface and the incoming and outgoing x-ray beam, respectively. $2\theta$ is the angle between incoming and outgoing beam and the offset $\Delta$ is typically 0.05°.
In order to perform contrast variation measurements, the

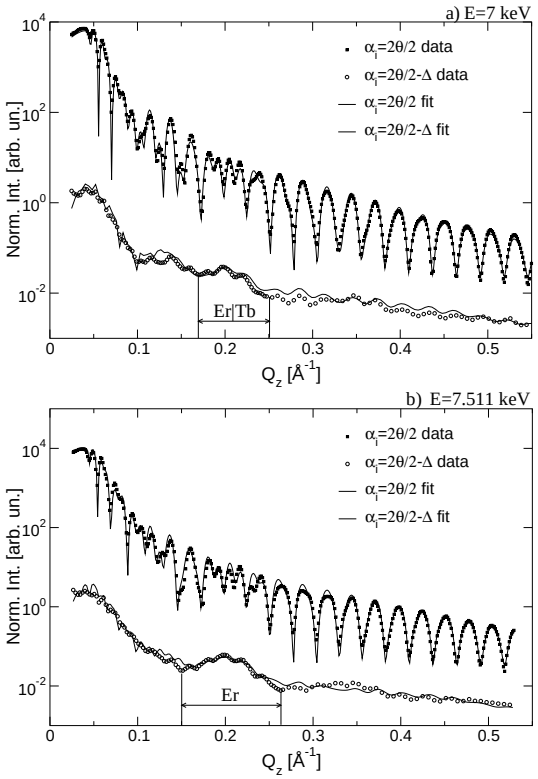


**Fig. 1.** Reflectivity ($\alpha_i = \frac{2\theta}{2}$) and longitudinal diffuse scattering ($\alpha_i = \frac{2\theta}{2} - \Delta$) from an [$Er_{43.5Å}$|$Tb_{36.1Å}$] bilayer capped with SiO measured at $E = 7$ keV (a) and $E = 7.511$ keV (b) as a function of $Q_z$. For small angles $\Delta$, $Q_z$ is given as: $Q_z \approx 2k \sin\left(\frac{2\theta}{2}\right)$. $\Delta Q_z$ corresponding to the thickness of the Er layer and the [Er|Tb] bilayer is indicated.

data were taken at the CEMO beamline of the HASYLAB, Hamburg. Measurements with the energy $E = 7.511$ keV close to the Tb $L_{III}$ absorption edge are sensitive to the interfaces between Er and Tb layers, since the contrast between the elements is enhanced due to anomalous scattering. Measurements at $E = 7$ keV highlight the interface between Tb and the Y buffer layer, while the contrast between Er and Tb is low.
Using this contrast variation, the properties of the different interfaces can be deduced. The results of the analysis of the reflectivity according to a Parratt formalism [12] confirm the nominal composition of the multilayers and yield an interface width between the rare earth layers of 8 to 13Å or 3 to 4.5 atomic layers in agreement with values reported for other rare earth superlattice systems [5, 13]. Similar values have been found for the superlattices by wide angle diffraction.
Beyond the reflectivity, the diffuse scattering at grazing incidence provides information on the lateral interface structure. Performing longitudinal diffuse scans, the scattering vector contains a component parallel to the sample surface. Therefore it probes lateral deviations from the ideal interface and their correlation within the interface or between different interfaces [14].
The diffuse scattering is surprisingly weak given the large

RMS interface width as deduced from reflectivity. Since interdiffusion and roughness lead to the same laterally averaged scattering length density profile —as is measured by reflectivity— while only the latter contributes to modulated diffuse scattering, we conclude that the interface width is partly due to interdiffusion. The discrepancy to the AES results can be understood, if the sensitivity of AES is taken into account. However, longitudinal correlations exist on different length scales as seen from the different oscillation in the longitudinal diffuse scans (see Fig. 1) from an [Er|Tb] bilayer. The energy independent short period oscillations are due to the Nb buffer layer. At lower $Q_z$ we observe two different length scales: If the contrast between Er and Tb is large, it roughly equals the thickness of a single Er layer. If the contrast vanishes, it matches the total thickness of the Er|Tb bilayer. This shows, that the interfaces in the rare earth system exhibit correlated fluctuations. Therefore, even the samples with layer thicknesses of 5 atomic layers have well separated Er and Tb layers.

We modeled the diffuse scattering data within the framework of the distorted wave Born approximation (DWBA) introduced by Sinha et al. [15] to the problem of surface roughness. This model was successfully applied to magnetic transition metal multilayers [16] and treats the interface broadening as roughness. Our refinements for the [Er|Tb] system are less satisfactory, probably due to the neglect of interdiffusion.

The $[\mathrm{Er}_{n_{\mathrm{Er}}}|\mathrm{Tb}_{n_{\mathrm{Tb}}}]$ superlattices —$n_{\mathrm{Er}}, n_{\mathrm{Tb}}$ denote the layer thicknesses in mono-atomic layers— have been characterised by wide angle x-ray diffraction XRD. Performing $\theta - 2\theta$ scans on a Bruker AX 8 x-ray reflectometer at large angles provides information about the crystalline order along the surface normal at room temperature. Using the approach of Schuller et al.[17–19], we deduce the respective $c_X$ lattice constants and averaged layer thicknesses in the framework of the program 'Suprex' by E. E. Fullerton. An example of such a XRD-scan together with the refinement is plotted for the $[\mathrm{Er}_{22}|\mathrm{Tb}_{22}]$ superlattice in Fig. 2. The results of this analysis are summarised in table 1.

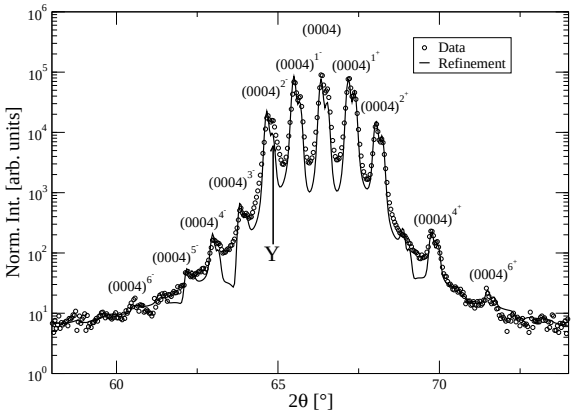


**Fig. 2.** XRD-scan and refinement for the $[\mathrm{Er}_{22}|\mathrm{Tb}_{22}]$ on a logarithmic scale: The superlattice peaks can be reproduced up to the 6th order. The deviations between fit and data close to the centre reflection might be due to thermal diffuse scattering, which is neglected in the model.

## 4 Magnetic structure

The magnetic phase diagram of the $[\mathrm{Er}_{n_{\mathrm{Er}}}|\mathrm{Tb}_{n_{\mathrm{Tb}}}]$ superlattices and the $\mathrm{Er}_{0.8}\mathrm{Tb}_{0.2}$ film have been investigated by neutron diffraction.

Neutron diffraction experiments were performed at the IN12 instrument of the Institute Laue-Langevin in Grenoble. The triple axis spectrometer provides a very low background level, and is therefore perfectly suited for the observation of small intensities as expected for scattering from thin films. At a neutron wave vector of 1.5 $\mathrm{Å}^{-1}$, a cooled Be filter was used to suppress the $\lambda/2$ contamination. The chosen collimator setup results in an instrumental resolution of 0.0012 $\mathrm{Å}^{-1}$ (FWHM).

The neutron diffraction data from the $\mathrm{Er}_{0.8}\mathrm{Tb}_{0.2}$ alloy film was collected at the DNS instrument of the research reactor FRJ2 in Jülich, which also provides a very good signal to noise ratio. At IN12 the samples were mounted into a LHe cryostat in order to vary the temperature between 5 K and room temperature. The temperature was controlled during the measurements to an accuracy better than 1 K. In Jülich we employed a closed cycle cryostat spanning the temperature range from 10 to 300 K with a comparable accuracy.

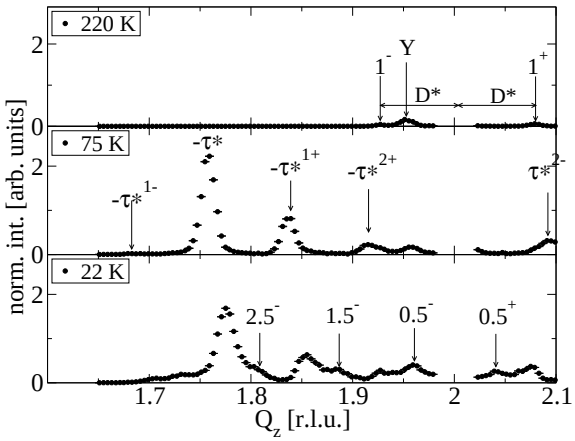


**Fig. 3.** Neutron diffraction from the $[\mathrm{Er}_{20}|\mathrm{Tb}_{5}]$ sample as a function of the $Q_z$ component of the scattering vector: The sample exhibits long range modulated magnetic order ($\tau^{*\pm l'}$) and antiferromagnetic coupling (AFc) of ferromagnetic (FM) layers ($\frac{2l'+1}{2}^{\pm}$) The (0002) Bragg reflection is cut for the sake of clarity.

The periodic alignment of the $4f$ magnetic moments leads to neutron scattering patterns as shown in Fig. 3, 5, if the scattering vector is scanned along $[000Q_z]$. The central (0002) Bragg reflection is cut for clarity in Fig. 3. The observed reflections can be classified as follows:

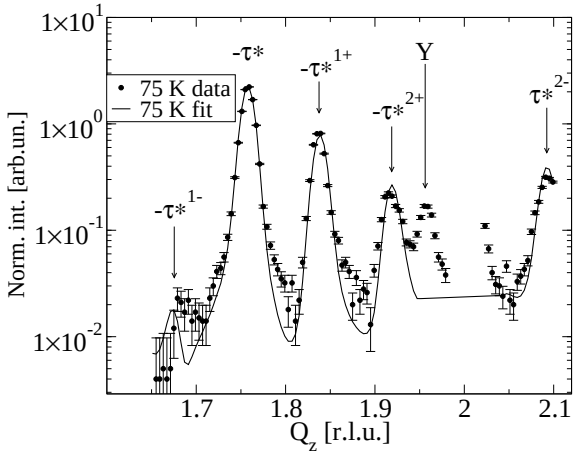


**Fig. 4.** Refinement of the neutron diffraction along the [000$l$] direction at 75 K together with the data on a logarithmic scale, using the model of Jehan et al. [13].

– The epitaxial growth together with the superlattice periodicity leads to reflections (the $z$-direction is again normal to the surface) [13]:

$$Q_z = \frac{4\pi l}{\overline{c}} \pm \frac{2\pi l'}{D} \tag{1}$$

$\overline{c}$ is the averaged $c$-lattice parameter and $D$ the averaged bilayer thickness, $l, l'$ integers. For $l' \neq 0$ the intensity depends on the contrast between Er and Tb layers, which is rather weak for nuclear scattering. The reflections are labelled with integers in Fig. 3 and 5.

– The incommensurate magnetic modulations as known from bulk rare earth elements produce reflections with a temperature dependent scattering vector:

$$Q_z = \frac{4\pi l}{\overline{c}} \pm \frac{2\pi l' \pm \Phi}{D} = \frac{4\pi l}{\overline{c}} \pm \left(\tau^* \pm \frac{2\pi l'}{D}\right) \tag{2}$$

$$\Phi = \sum_{i}^{bilayer} \phi_i \,. \tag{3}$$

$\phi$ represents the turn angle between neighbouring monolayers, $\Phi$ the accumulated turn angle across one bilayer and $\tau^*$ the respective propagation vector modulo $2\pi$. For the [$Er_{20}$|$Tb_5$] superlattice, these reflections appear below 150 K. Using the model of Jehan [13] for temperatures 80 K $< T <$ 150 K, the observed spectra can be reproduced assuming turn angles $\phi_{Er}$ of 51 in the centre of a Er layer and $\phi_{Tb}$ 18- 23 in the centre of a Tb layer (see Fig. 4). We had to fix either of these parameters, since the correlation between the two is very strong. A good agreement for all temperatures above 80 K could be found by fixing the Er value to its bulk value at 80 K. The fitted values of the Tb turn angle cover the same range as in the helix phase of bulk Tb. The very weak intensity of the $-\tau^{*1-}$ satellite can be reproduced within this simple model only, if we assume a non vanishing magnetic moment in both layers, Er and Tb. The magnetic moment inside the Er layer is smaller than the moment in the Tb layer. Absolute values cannot be achieved, since the coherence length for nuclear and magnetic scattering differ strongly. Therefore the magnetic intensity cannot be normalized to the nuclear one. To determine the averaged magnetization density within the layers, the intensity around a larger number of main Bragg reflections has to be measured.

If the modulation is not coupled across several bilayers, we observe instead broad diffuse intensity from incoherent scattering of single layers (cp. Fig. 5). This intensity is centred around $Q_z$ defined by

$$Q_z = \frac{4\pi l}{c_X} \pm \frac{2\phi}{c_X} = \frac{4\pi l}{c_X} \pm \tau^*, \tag{4}$$

$c_X$ denoting the $c$-lattice constant in the respective material and $\phi$ the phase angle between neighbouring atomic layers. Such a broad feature we observe in all superlattices containing Tb layers thicker than 5 atomic layers.

– Ferromagnetically ordered layers couple antiferromagnetically. For this magnetic structure the superlattice periodicity is doubled:

$$Q_z = \frac{4\pi l}{\overline{c}} \pm \frac{2\pi(2l'+1)}{2D} \tag{5}$$

The respective reflections are labelled with half integer indices. These reflections appear in all superlattices. For the [$Er_{20}$|$Tb_5$] superlattice, they set in at temperatures below 60 K with a huge thermal hysteresis. They coexist with the $\tau^{*l^{\pm}}$ peaks down to lowest temperatures, probably featuring ferromagnetic and helical domains. For thicker Tb layers, the ferromagnetic order appears at $T = 230$ K, i.e. $T_N$ of bulk Tb.

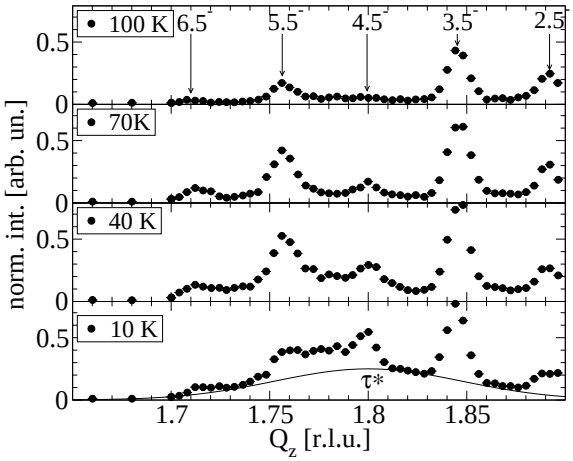


**Fig. 5.** Neutron diffraction from the [$Er_{22}$|$Tb_{22}$] sample as a function of the $Q_z$ component of the scattering vector: High order reflections due to AFc of FM layers ($\frac{2l'+1}{2}^{\pm}$) and broad diffuse scattering due to short range modulated magnetic order ($\tau^*$).

The different components of the ordered magnetic moment can be separated by analysing the $\boldsymbol{Q}$ dependence of the

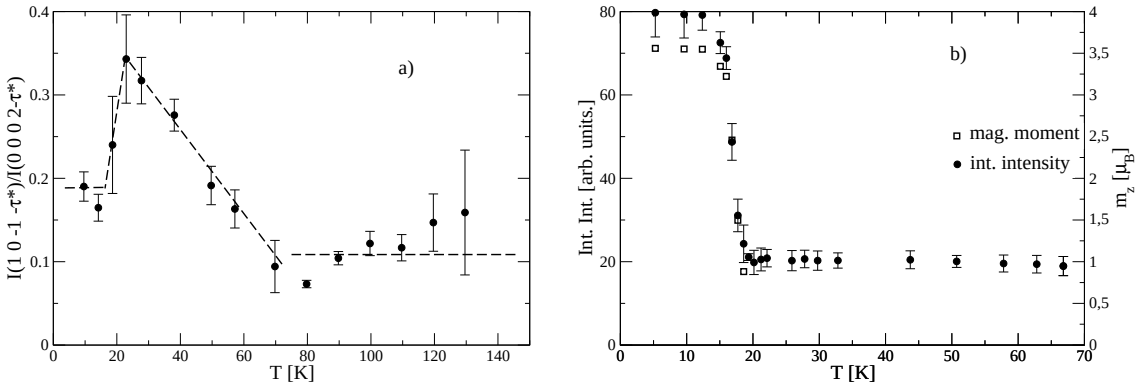


**Fig. 6.** a) Ratio of the integrated intensities for the incommensurate magnetic reflections $(10\overline{1}-\tau^*)$ and $(0002-\tau^*)$. The dashed line is a guide to the eye. b) Integrated intensity of the $(10\overline{1})$ reflection and ferromagnitcally ordered c-axis component of the magnetic moment (right ordinate).

magnetic reflections. Reflections of type $(000Q_z)$ contain only information about the basal plane magnetic moment, since only the component perpendicular to the scattering vector contributes to magnetic neutron scattering. Additional measurements of $(10\overline{1}Q_z)$ reflections allows one to obtain the $c$-axis component. Long range ordering of the $c$-axis component was found only for the $Er_{0.8}Tb_{0.2}$ alloy and the $[Er_{20}|Tb_5]$ superlattice. For the superlattice, we compared the intensities for the incommensurate peaks $(10\overline{1}-\tau^*)$ and $(0002-\tau^*)$, taking into account the Lorentz factor [20] and the magnetic form factor [21] (Fig. 6). Below 80 K the ratio increases due to the onset of the modulated order of the c-axis component. At 20 K the ratio drops again, accompanied by a drastic increase of intensity of the $(10\overline{1})$ Bragg peak, featuring the transition to the cone structure. The width of this peak is purely defined by the instrumental resolution like the nuclear Bragg peaks. By normalising to the nuclear scattering intensity we find a ferromagnetically ordered $c$-axis moment of 3.5(3) $\mu_b$, that is reduced from the bulk moment of 7.9 $\mu_B$ [22]. We emphasise the long range order of the c-axis component, that leads to more intense superlattice satellites due to the increased contrast (see Fig. 7). In the case of the superlattice, the phase transition temperatures for the c-axis component remain unchanged with respect to metallic Er and within the accuracy of the measurements (cp. Fig. 8). The sequence of the different phases depends strongly on the composition of the superlattice. Magnetic phases and phase transition temperatures are summarized in the schematic phase diagram Fig. 8 for our different samples and for the pure elements [23]: The samples with a Tb thickness larger than 5 atomic layers order ferromagnetically within a single Tb layer, stacked in antiferromagnetic order. The long range helix cannot be detected in these samples. The ferromagnetic transition temperature is identical to the Néel- temperature in bulk Tb. Long range modulated structures are found in the $Er_{0.8}Tb_{0.2}$ alloy and $[Er_{20}|Tb_5]$ superlattice. A helical phase is observed below 150 K in the superlattice. At 80 K, i. e. $T_N$ of Er, an ordered $c$-axis component appears. This component orders ferromagnetically at $T_C = 20$ K, approximately the $T_C$ of bulk Er. The onset of a helical magnetic structure at a higher temperature than the onset of the $c$-axis modulation reminds on the phase diagram of $Er_xTb_{1-x}$ alloys [24]. Since the interfaces between Er and Tb are not atomically sharp and flat, alloy like phases might be present at the interfaces. The magnetic properties of the $[Er_{20}|Tb_5]$ superlattice are nevertheless substantially different from the $Er_{0.8}Tb_{0.2}$ alloy, that contains the same relative amounts of Er and Tb.

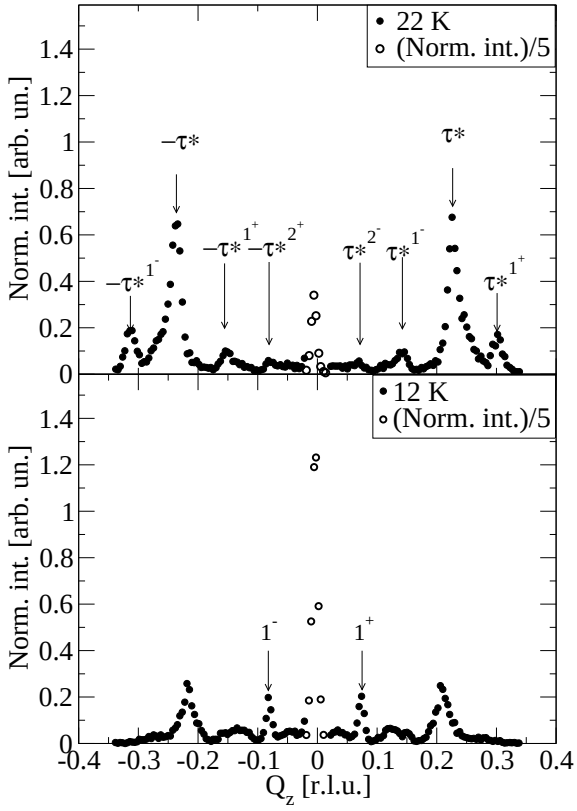


**Fig. 7.** Neutron diffraction spectra $(10\overline{1}Q_z)$ above and below the ferromagnetic ordering of the $c$-component of the magnetic moment. In the region $-0.02 < Q_z < 0.02$ r.l.u., the intensity is divided by 5 for clarity.

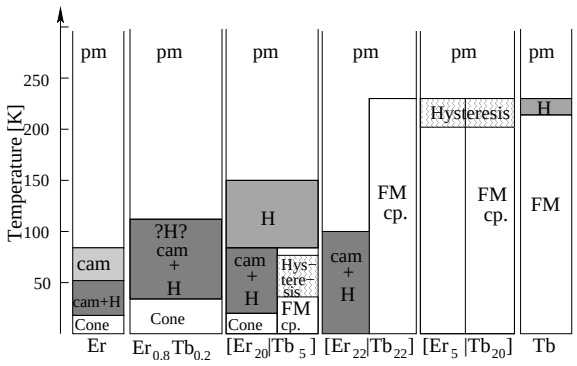


**Fig. 8.** Schematic phase diagram for the series of [Er|Tb] superlattices and the $Er_{0.8}Tb_{0.2}$ alloy studied by wide angle neutron diffraction. CAM refers to the c-axis modulated structure and H to the pure helix. Long range coupled order is indicated by cp. For the $[Er_{22}|Tb_{22}]$ sample, the combination of the CAM structure and the pure helix order is only short range.

## 5 XRES

X-ray resonance exchange scattering can occur, if the photon energy is tuned close to some absorption edges of magnetic elements [25]. Complementary to neutron diffraction, XRES probes electronic states above the Fermi energy, which are spin polarised in magnetically ordered systems. It offers a unique possibility to study the magnetic properties of the superlattice element specific. XRES can be described as a second order perturbation process, which involves the virtual excitation of a core level electron into an empty state with subsequent decay and reemission of a photon [25]. The scattered intensity depends on the density of states above the Fermi level, which is exchange split in magnetic materials. The resonance enhancement is a result of the vanishing real part of the energy denominator in second order perturbation theory. Furthermore the polarisation of the scattered photons yields information about the intermediate states involved in the scattering process. Performing full polarisation analysis, Sanyal et al. [26] and Perry et al. [27] have shown that the dominant contribution to XRES at the Er and Tb $L_{III}$ edges stems from transitions $2p \rightarrow 5d$. Hence XRES probes mainly the polarisation of the conduction band electrons at the $L_{III}$ edge of the rare earth metals. These electrons are supposed to mediate the interlayer coupling.

Experiments were performed at the 6ID-B beamline of the APS. The high flux and the high $\boldsymbol{Q}$-resolution allows a detailed study of the temperature dependence of the propagation vector $\tau^*$ and reflection width. While the neutron data is resolution limited and the reflections overlap strongly, the different features can be better resolved by XRES.

Fig. 9 compares the diffraction pattern at the $L_{III}$ edge of Er and Tb, respectively, for the $[Er_{20}|Tb_5]$ sample. Because of the strong charge scattering background we performed the experiment in $\sigma \rightarrow \pi$ geometry only, i.e. the polarisation of the incoming light is perpendicular to the scattering plane ($\sigma$ polarisation), while the scattered light is polarised parallel to the scattering plane ($\pi$ polarisation). In contrast to charge scattering, which conserves the polarisation, the magnetic scattering can rotate it [28, 29]. Using the (006) reflection of a pyrolytic graphite crystal suppressed the charge scattering at the Er $L_{III}$ edge by 95 %, as the analyser $2\theta$ angle is 85 degree. The Al (222) reflection yielded a charge scattering suppression of more than 99 % at the Tb $L_{III}$ edge ($2\theta \approx 90$ degree), which is mainly due to the high degree of horizontal linear polarisation of the incoming x-ray beam. Therefore we have to measure around the (0004) Bragg reflection at the Er $L_{III}$ edge, where the charge scattering is reduced due to the atomic form factor.

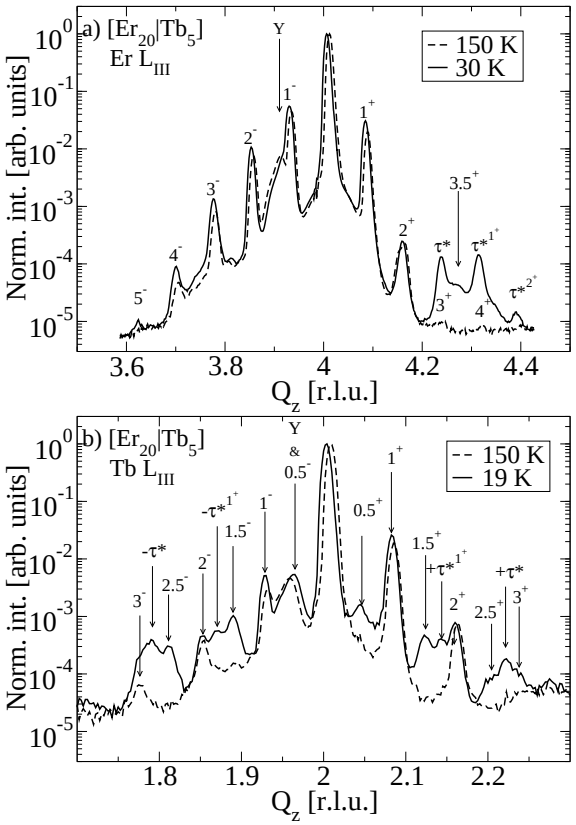


**Fig. 9.** XRES as a function of $Q_z$ measured in $\sigma \rightarrow \pi$ geometry at different temperatures, normalised to the maximum intensity: a) XRES from the $[Er_{20}|Tb_5]$ sample close to the Er $L_{III}$ absorption edge ($E = 8.361$ keV); b) XRES from the $[Er_{20}|Tb_5]$ sample close to the Tb $L_{III}$ absorption edge ($E = 7.518$ keV).

For the $[Er_{20}|Tb_5]$ sample we observe the same type of reflections at both absorption edges (Er $L_{III}$ and Tb $L_{III}$). The temperature dependence of the modulation wave vector is shown in Fig. 10 along with the neutron data for the $[Er_{20}|Tb_5]$ sample. The x-ray data is taken from measurements at the Tb $L_{III}$ edge. The propagation vectors derived from the neutron and x-ray data show the same variation with temperature (Fig. 10).

The width of the magnetic reflections is determined completely by the coherence length of the spin polarisation

for the x-ray data, the instrumental resolution can be neglected. We deduce a coherence length $\zeta = \frac{2\pi}{\Delta Q_z} \approx 350$ Å or 5 bilayers. The same behaviour is observed for antiferromagnetic coupling of FM layers. With the onset of the FM order the intensity of the reflection due to modulated magnetic order decreases (Fig. 11). For both types of reflections we observe complementary hysteresis loops as a function of temperature. The resonance behaviour shown

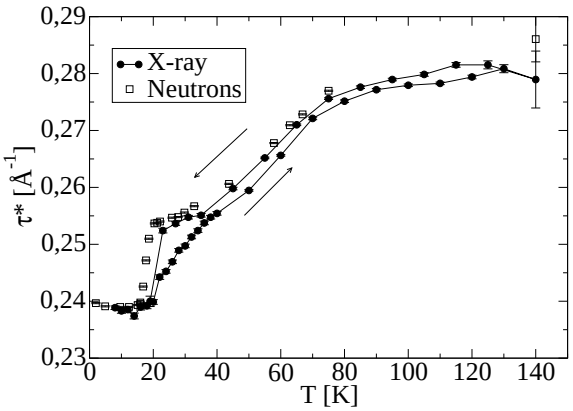


**Fig. 10.** Single peak analysis of the the reflections in Fig. 9 b) as a function of temperature: Modulation wave vector $\tau^*$ determined at the Tb $L_{III}$ absorption edge $E = 7.518$ keV. The neutron results are also shown.

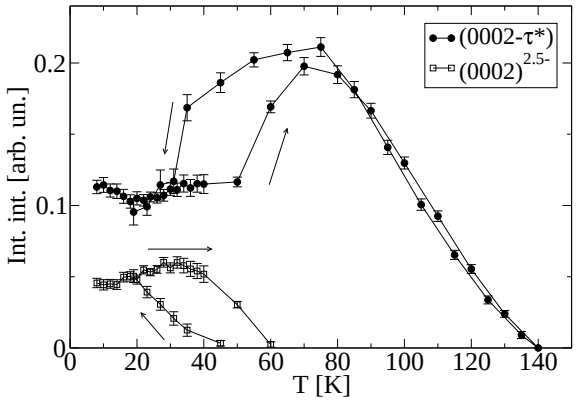


**Fig. 11.** Single peak analysis of the the reflections in Fig. 9 b) as a function of temperature: Integrated intensities of the $\tau^*$ and the $2.5^-$ reflection measured at $E = 7.518$ keV.

in Fig. 12 confirms the magnetic origin for the modulation type reflections and the half integer superlattice satellites. The double peak structure, clearly resolved at the Er $L_{III}$ edge, has not been observed in the earlier study of bulk Er [26], possibly due to a insufficient energy resolution. At the Tb $L_{III}$ edge, Perry et al. [27] observed a similar resonance behaviour, when they studied the helix phase of metallic Tb at 226 K.

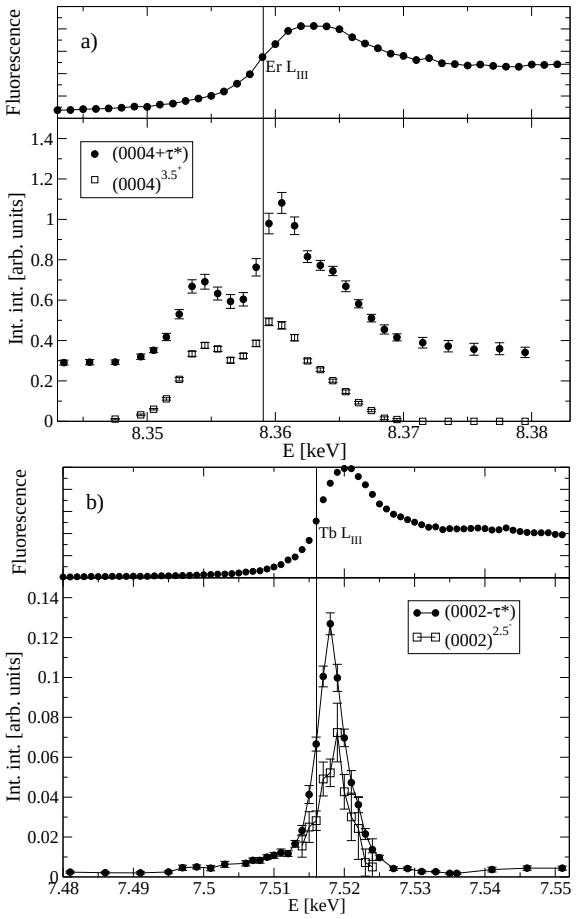


**Fig. 12.** Energy dependence of the integrated intensity: a) close to the Er $L_{III}$ edge, $T = 30$ K, b) close to the Tb $L_{III}$ edge, $T = 12$ K. The fluorescence yield in the upper part gives a measure for the respective edge position.

In contrast, the $[Er_{22}|Tb_{22}]$ sample has a qualitative different diffraction pattern at the two absorption edges, shown in Fig. 13 a) and b). At the Er $L_{III}$ edge we observe a broad diffuse intensity $\tau^*$ at low temperature, related to the short range magnetic modulation (cp. fig 14). The width of the feature, as deduced by a Gaussian fit, equals the reciprocal Er layer thickness. On top of the broad feature, a series of sharp reflections appears at low temperature (see Fig. 14). They can be identified as integer and half integer superlattice satellites. On heating, the broad feature and the sharp reflection disappear both roughly at 80 K. This is consistent with the loss of magnetic order for bulk Er at this temperature: also in the multilayer we do not observe magnetic short or long range order in Er above this temperature. The resonance behaviour at the Er $L_{III}$ edge shown in Fig. 15 is different for the half integer and integer superlattice satellites: while the half integer satellites resonate as expected for a magnetic origin, the integer satellites show the increased absorption of a charge reflection. The resonance shape of the magnetic reflections is the same as for the $[Er_{20}|Tb_5]$ superlattice. When magnetic ordering occurs inside the Er layer, we assume that the ferromagnetic Tb layer induces ferromagnetic order

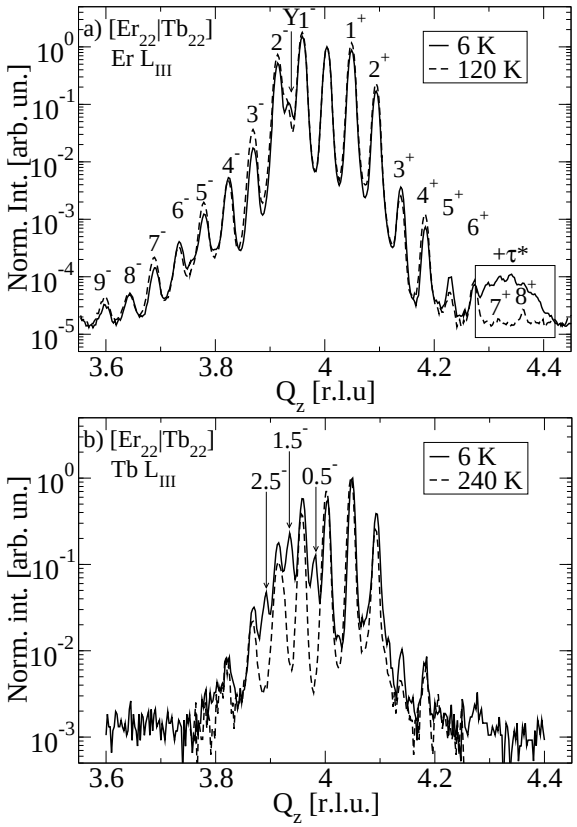


**Fig. 13.** XRES as a function of $Q_z$ measured in $\sigma \rightarrow \pi$ geometry at different temperatures, normalised to the maximum intensity: a) XRES from the [$Er_{22}$|$Tb_{22}$] sample close to the Er $L_{III}$ absorption edge ($E$ = 8.361 keV); b) XRES from the [$Er_{22}$|$Tb_{22}$] sample close to the Tb $L_{III}$ absorption edge ($E$ = 7.518 keV).

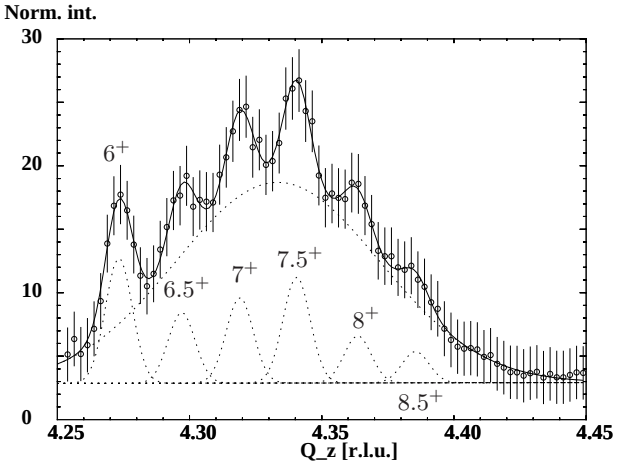


**Fig. 14.** Single peak analysis of the part of the diffraction pattern inside the box in Fig. 13 a).

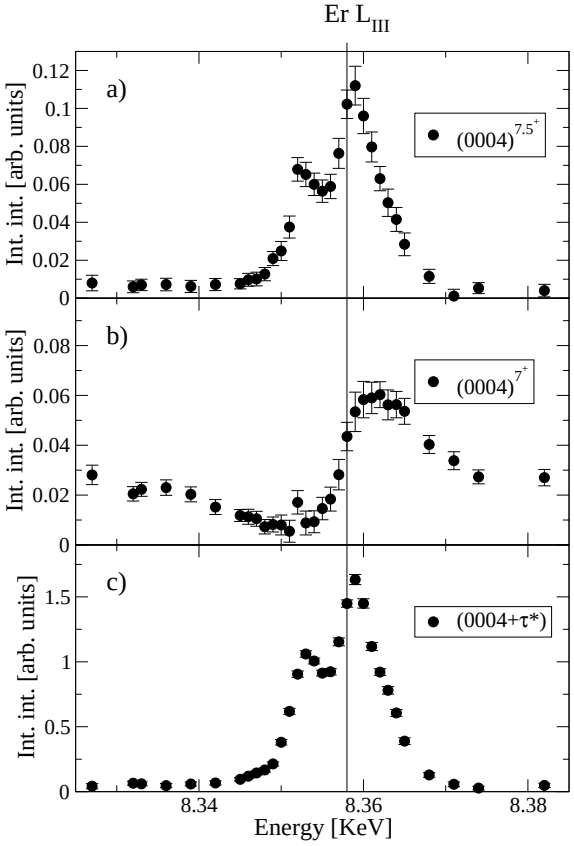


**Fig. 15.** Energy dependence of integrated intensities close to the Er $L_{III}$ edge from [$Er_{22}$|$Tb_{22}$] superlattice,$T$ = 9 K: a) $(0004)^{7.5^+}$, b)$(0004)^{7^+}$, c) $(0004 + \tau^*)$, the broad component of the fit shown in Fig. 14. The absorption edge is determined by a fluorescence yield measurement.

at the interface, while the centre adopts the bulk Er-like modulated magnetic structure. The modulated structure is only short range, while the interfacial order follows the long range coupling of the Tb layers.

At the Tb $L_{III}$ edge, the $\frac{2l'+1}{2}$ reflections due to antiferromagnetic coupled FM layers appear below 230 K ( see Fig. 15 b). The reflections can be detected for the whole temperature range of the FM phase despite the strong charge scattering background close to the (0004) central reflection. The width of the reflection is about the same as the width of the structural reflections. The range of magnetic order along the growth direction is therefore comparable to the range of structural order.

An [$Er_{20}$|$Tb_{10}$] sample, that has been studied only by XRES, behaves in a similar way. Short range modulated correlations are found at the Er edge, while long range FM spin polarisation is observed for energies close to the Tb edge. We detect hints to ferromagnetic coupling as well as to antiferromagnetic coupling. However, to draw conclusions on the magnetic structure for this sample, the neutron diffraction data is required.

The XRES from the $Er_{0.8}Tb_{0.2}$ alloy film is very intense (up to 50000 counts per second) and not obscured by the superlattice reflections. We studied the temperature and energy dependence of the magnetic modulation at the peak $(0002 - \tau^*)$ (Fig. 16 and 17). The onset of XRES intensity coincides with the Néel temperature found by neutron diffraction. However, the integrated intensity shows two kinks as a function of temperature, one at 60 K and a second at 22 K. These are correlated with a significant increase of the peak width, that corresponds to a decrease of the correlation length. Both, the correlation length along the growth direction and in-plane are lowered in this temperature range. The modulation vector shows a small tendency of a hysteresis. For single crystals of the same composition Millhouse et al. [24] observed a stronger hysteresis and also slightly different phase transition temperatures, that can be explained by the epitaxial strains in the film. The resonances at the Er and at the Tb edge have the same shape as in the case of the superlattice samples.

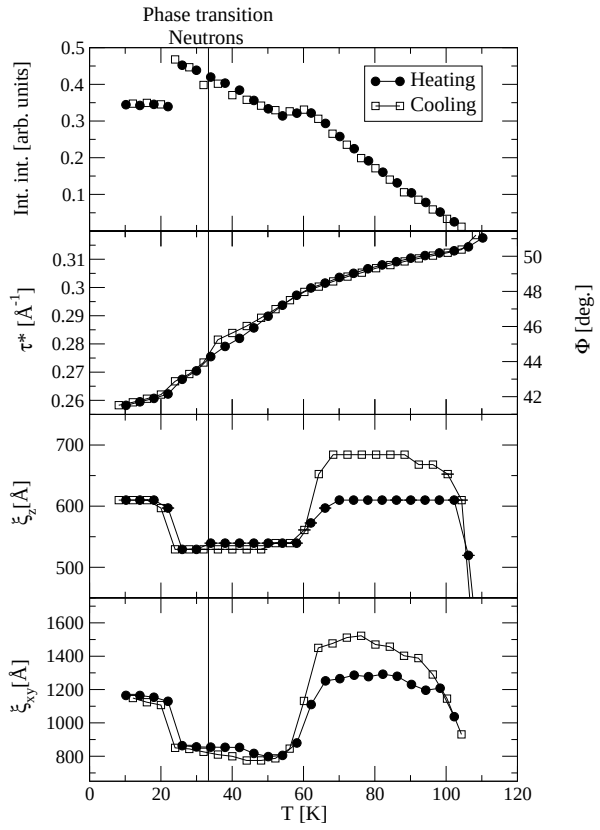


**Fig. 16.** Temperature dependence ($T = 10$ K) of the magnetic modulation peak $(0002-\tau^*)$ in the $Er_{0.8}Tb_{0.2}$ film, determined at $E = 8.359$ keV, i.e. the Er $L_{III}$ edge. Integrated intensities have been determined performing rocking scans across the reflection. The vertical correlation length $\zeta_z$ is deduced from the width of longitudinal scans $[000q_z]$, the in-plane correlation length is deduced from the width of the rocking scans, which correspond roughly to transverse scans in reciprocal space.

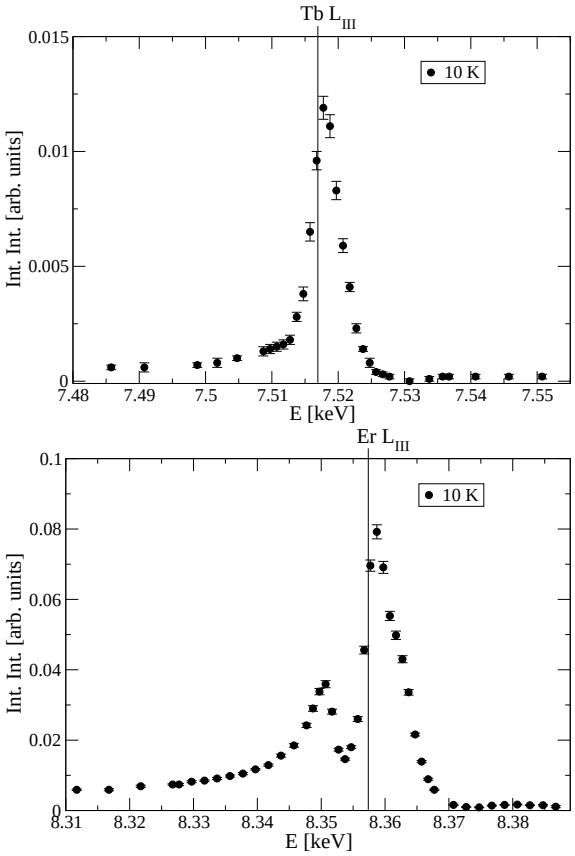


**Fig. 17.** Energy dependence ($T = 10$ K) of the magnetic modulation peak $(0002 - \tau^*)$ in the $Er_{0.8}Tb_{0.2}$ film. Integrated intensities have been determined performing rocking scans across the reflection.

## 6 Discussion

Neutron diffraction from a series of superlattices show basal plane ferromagnetic ordering for all investigated samples, assumed to occur mainly in the Tb layers. The phase transition temperatures for this structure depend on the thickness of the Tb layer. If the Tb layer thickness is greater than 20 mono-atomic layers, the ordering sets in at $T_N$ of bulk Tb. The suppression of the helix phase in Tb and Dy containing superlattices has been explained in terms of compressive strains due to the epitaxy on the smaller ions for other rare earth superlattices [30,6,3]. With XRES, we observe weak Fourier components according to the ferromagnetic order in Er below the ordering temperature of bulk Er, too (cp. Fig. 12, 15). We attribute this to an induced order at the interface to the Tb layers, while the exchange energy, that defines the phase transition temperature, is not changed significantly from the bulk Er value. For Tb thicknesses smaller than 10 mono-atomic layers ferromagnetic order of the basal plane is observed only for temperatures below 60 K with a strong thermal hysteresis.

Long range ordered, modulated magnetic structures exist only in the $[Er_{20}|Tb_5]$ sample below 150 K. For the other samples we observe modulated phases without any coupling between neighbouring layers roughly below 80 K.

Long range order of the $c$-axis component occurs in the $[Er_{20}|Tb_5]$ superlattice. To our knowledge this is observed for the first time in a Rare Earth superlattice. The phase transition temperatures are similar to the $c$-axis ordering in bulk Er. In the other samples we observe a short range modulated $c$-axis component. The transition to a ferromagnetic alignment of the $c$-component is suppressed in that cases. The neutron diffraction data indicates a coexistence of a modulated magnetic phase with antiferromagnetically coupled ferromagnetic layers in the $[Er_{20}|Tb_5]$ sample. According to the XRES data, the modulated and the ferromagnetic structures are present in both, the Er and the Tb layers, since corresponding superlattice reflections were observed at th $L_{III}$ resonances of both elements. Combining neutron diffraction and XRES results indicates that 4f and 5d electronic states show as well modulated as ferromagnetic order. Since these two ordering phenomena are mutually exclusive, they can be realized only as an incoherent superposition, i.e. a laterally inhomogeneous state. From transversal $Q_x$ scans, which were found to be resolution limited, we can conclude, that the corresponding domains are rather large ($> 800$ Å). Such a model of a laterally inhomogeneous magnetic state could also explain the large hysteresis effects at low temperature. One could argue, that domain growth processes are limited by structural imperfections at the interfaces which act as pinning centres. To clarify this issue, we recently studied the diffuse scattering of polarized neutrons at grazing incidence [31]. Our structural characterisation shows, that the interfaces are not atomically flat, but exhibit strongly vertically correlated roughness. Therefore the nearest neighbour arrangement is highly anisotropic:
along the growth direction a sequence of atoms corresponding to the nominal layer composition is closely followed. In the lateral directions a nearly random alloy is realized in the two interface regions of each layer, see the schematic in Fig. 18. Thus, the interfacial region can be viewed as a 'structurally highly anisotropic alloy'. In the $[Er_{20}|Tb_5]$ superlattice, this anisotropic alloy extends through the whole Tb layer. The strong structural anisotropy in the interface region leads to a significantly different phase diagrams for the layered system and the alloy with the same nominal composition (20 % Tb, 80 % Er). To derive quantitative conclusions about the magnetization distribution, e.g. the decay of a given magnetic structure in one of the layers, it would be necessary to observe a larger number of main Bragg reflections.

If the Tb layer thickness becomes bigger, we observe different spin polarisations for each element. The diffuse XRES at the Er $L_{III}$ edge points to a short range magnetic modulation restricted to a single Er layer. At the Tb $L_{III}$ edge we were able to observe the spin polarisation according to an antiferromagnetic coupling of ferromagnetically ordered layers because of the strong suppression of the charge scattering by the polarisation analysis. The gain of magneto elastic energy due to compressive strains becomes more important for thicker Tb layers and leads to the ferromagnetic phases. The ferromagnetic Tb layers can couple via magnetic dipolar interactions [6], leading to the antiferromagnetic coupling, even if the Er thickness is as big as 20 mono-atomic layers.

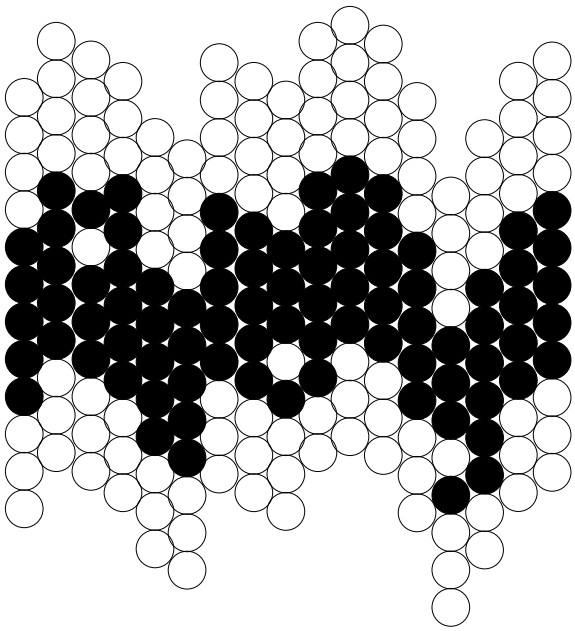

**Fig. 18.** Schematic view of a single layer with the two interface regions, cut along the growth direction and one lateral direction. Correlated structural roughness is combined with some degree of interdiffusion.

## 7 Summary and conclusion

We have investigated the structural and magnetic properties of [Er|Tb] multilayers. The interface roughness is vertically correlated as can be seen from the longitudinal oscillations in the diffuse x-ray scattering under grazing incidence. From the reflectivity we get an upper limit for the interface extension of 3-4 mono-atomic layers. Since this is partly caused by correlated roughness, the sequence of atoms along the growth direction may still correspond to the nominal composition, even if the layer thickness becomes as small as 5 atomic layers. This conclusion is supported by the different magnetic behaviour of the $Er_{0.8}Tb_{0.2}$ alloy and the $[Er_{20}|Tb_5]$ superlattice, in which the nominal Tb layer can be considered as a highly anisotropic alloy.

The system shows different magnetic structures depending on the composition of the superlattice. Antiferromagnetic coupling of ferromagnetic layers is present in all samples, while long range incommensurate magnetic modulations appear only in the $[Er_{20}|Tb_5]$ superlattice. The effect of the artificial superstructure is emphasised by the comparison between the $Er_{0.8}Tb_{0.2}$ alloy and the $[Er_{20}|Tb_5]$ superlattice. While the former shows modified phase transition temperatures as compared to the bulk alloy and a common conduction band polarisation, new magnetic structures appear in the superlattice, e.g. the basal plane ferromagnetism in Er due to the anisotropic

alloying at the interface. In this superlattice, we observe long range ordering of the *c*-axis component of the magnetic moment. To our best knowledge this was observed for the first time in Rare Earth superlattices. The coupling of ferromagnetic layers could be mediated via dipolar interactions leading to an antiferromagnetic coupling of ferromagnetic Tb layers, which is observed in the samples containing thicker Tb layers.

In conclusion, the effect of competing anisotropies is to break up long range order due to exchange interactions for larger thicknesses. A coherent magnetic order is established for the basal plane and the *c*-axis component if the nominal Tb layer is sufficiently thin (5 monolayers) and the different interface regions join.

We thank J. Thelen for the technical support during the sample preparation and E. Zoellner and D. S. Robinson for technical support and fruitful discussions during the beamtime at the APS. Use of the Advanced Photon Source was supported by the U.S. Department of Energy, Basic Energy Sciences, Office of Science, under Contract No. W-31-109-Eng-38. The MUCAT sector at the APS is supported by the Department of Energy, Office of Science through the Ames Laboratory contract No. W-7405-Eng-82.

## References

1. M. B. Salamon, S. Sinha, J. J. Rhyne, J. E. Cunningham, R. W., E., J. Borchers, C. P. Flynn, *Phys. Rev. Lett.*, **56**, 259 (1986).
2. C. F. Majkrzak, J. W. Cable, J. Kwo, M. Hong, D. B. McWhan, Y. Yafet, J. V. Waszczak, C. Vettier, *Phys. Rev. Lett.*, **56**, 2700 (1986).
3. R. A. Cowley, *J.M.M.M.*, **177-181**, 1156 (1998).
4. K. Dumesnil, C. Dufour, Ph. Mangin, G. Marchal, M. Hennion, *Phys. Rev. B*, **54**, 6407 (1996).
5. J. A. Simpson, D. F. McMorrow, R. A. Cowley, R. C. C. Ward, M. R. Wells, *Z. Phys. B*, **101**, 35 (1996).
6. C. Bryn-Jacobsen, R. A. Cowley, D.F. McMorrow, J. P. Goff, R. C. C. Ward, M. R. Wells, *Phys.Rev.B*, **55**, 14360 (1997).
7. J. Voigt, E. Kentzinger, U. Rücker, W. Schweika, W. Schmidt, D. Hupfeld, D. Wermeille, Th. Brückel, *Europhys. Lett.*, **65**, 4, 560 (2004).
8. D. Gibbs, J. Bohr, J. E. Axe, D. D. Moncton, K. L. D'Amico, *Phys. Rev. B*, **34**, 8182 (1986).
9. C. F. Majkrzak, J. Kwo, M. Hong, Y. Yafet, D. Gibbs, C. L. Chien, J. Bohr, *Adv. Phys.*, **40**, 99 (1991).
10. W. Babik, Grenzflenmorphologie von GMR und TMR-Schichtsystemen, Ph.D. thesis, RWTH Aachen (2002).
11. J. Kwo, G. K. Wertheim, M. Gurvitch, D. N. E. Buchanan, *IEEE Trans. Mag.*, **Mag-19**, 795 (1983).
12. L. G. Parrat, *Phys. Rev.*, **95**, 359 (1954).
13. D. A. Jehan, D. F. McMorrow, R. A. Cowley, M. R. Wells, R. C. C. Ward, K. N Clausen, *Phys. Rev. B*, **48**, 5594 (1993).
14. H. Zabel, *Appl. Phys. A*, **58**, 159 (1994).
15. S. Sinha, E. B. Sirota, S. Garoff, H. B. Stanley, *Phys. Rev. B*, **38**, 2297 (1988).
16. S. Nerger, E. Kentzinger, U. Rücker, J. Voigt, F. Ott, H. Seeck O., Th. Brückel, *Physica B*, **297**, 185 (2001).
17. I. K. Schuller, *Phys. Rev. Lett.*, **44**, 1597 (1980).
18. E. E. Fullerton, I. K. Schuller, H. Vanderstraeten, Y. Bruynserade, *Phys. Rev. B*, **45**, 9292 (1992).
19. W. Sevenhans, M. Gijs, Y. Bruynserade, H. Homma, K. Schuller I., *Phys. Rev. B*, **34**, 5955 (1986).
20. G. M. McIntyre and R. F. D. Stansfield, *Acta. Cryst. A*, **44**, 257 (1988).
21. P. J. Brown, *International Tables of Crystallography C* (1983).
22. J. W. Cable and E. O. Wollan and W. C. Koehler and M. K. Wilkenson, *Phys. Rev.*, **140**, 1896 (1965).
23. J. Jensen, A. R. Mackintosh, *Rare earth magnetism* (Oxford University Press, Oxford, 1991).
24. A. H. Millhouse and W. C. Koehler, *Intern. J. Magnetism*, **2**, 389 (1971).
25. J. P. Hannon and G. T. Trammel and M. Blume and D. Gibbs, *Phys. Rev. Lett.*, **61**, 1245 (1988).
26. M. K. Sanyal, D. Gibbs, J. Bohr, M. Wulff, *Phys.Rev.B*, **49**, 1049 (1994).
27. S. C. Perry, M. M. R. Costa, W. G. Stirling, J. R. Longfield, D. Mannix, Th. Brückel, *J.Phys.Cond.Mat.*, **10**, 1951 (1998).
28. M. Blume and D. Gibbs, *Phys. Rev. B*, **37**, 1779 (1988).
29. J. P. Hill and D. F. McMorrow, *Acta Cryst. A*, **52**, 236 (1996).
30. R. S. Beach, J. A. Borcher, A. Matheny, M. B. Salamon, B. Everitt, K. Pettit, J. J. Rhyne, C. P. Flynn, *Phys. Rev. Lett.*, **70**, 3502 (1993).
31. J. Voigt, E. Kentzinger, U. Rücker, A. Paul, T. Brückel, *to be published*.

| Sample | # of bilayers | $\overline{n}_{\mathrm{Er}}$ | $\overline{n}_{\mathrm{Tb}}$ | $D$[Å] | $c_{\mathrm{Er}}$[Å] | $c_{\mathrm{Tb}}$[Å] | Mosaic spread FWHM [°] |
|---|---|---|---|---|---|---|---|
| $[Er_{22}\|Tb_{22}]$ | 80 | 22.2(3) | 22.0(3) | 124.5(5) | 5.556(1) | 5.714(2) | 0.20 |
| $[Er_{20}\|Tb_{10}]$ | 63 | 19.6(1) | 10.8(1) | 85.0(5) | 5.574(1) | 5.708(2) | 0.24 |
| $[Er_{20}\|Tb_{5}]$ | 150 | 21.2(3) | 5.0(3) | 73.5(5) | 5.590(1) | 5.72(1) | 0.21 |
| $[Er_{5}\|Tb_{20}]$ | 120 | | | 73(2) | | | 0.20 |
| $Er_{0.8}Tb_{0.2}$ | | | | | | | 0.11 |

**Table 1.** Structural parameters of the different superlattices deduced from XRD. The values are results from modelling with the 'Suprex' program, see Ref. [18] for details. D is the bilayer thickness, $c_{\mathrm{Er}}$ and $c_{\mathrm{Tb}}$ are the c-axis lattice parameters within the Er and Tb layers, respectively. Additionally the mosaic spread is given.